Combustion and Flame 240 (2022) 111960

Contents lists available at ScienceDirect

Combustion and Flame

journal homepage: www.elsevier.com/locate/combustflame

Experimental and numerical analysis of fine particle and soot formation in a modern 100 MW pulverized biomass heating plant

Niko P. Niemelä[a,*], Fanni Mylläri[a], Niina Kuittinen[a], Minna Aurela[b], Aku Helin[b], Joel Kuula[b], Kimmo Teinilä[b], Markus Nikka[c], Oskari Vainio[c], Anssi Arffman[c], Henna Lintusaari[a], Hilkka Timonen[b], Topi Rönkkö[a], Tero Joronen[a]

[a] Faculty of Engineering and Natural Sciences, Tampere University, Korkeakoulunkatu 6, 33720, Tampere, Finland
[b] Atmospheric Composition Research, Finnish Meteorological Institute, Erik Palménin aukio 1, 00560, Helsinki, Finland
[c] Dekati Ltd., Tykkitie 1, 36240, Kangasala, Finland

ARTICLE INFO

Article history:
Received 14 May 2021
Revised 15 December 2021
Accepted 22 December 2021

Keywords:
Biomass
Pulverized fuel
Combustion
Fine particles
Soot
Fouling

ABSTRACT

The formation of soot, organic, and inorganic aerosols has a profound effect on the environmental and technological feasibility of biomass combustion. In this work, the soot and aerosol processes are examined for a modern pulverized wood-burning 100 MW_{th} district heating plant. Experimental data was collected from two locations inside the furnace (30% and 100% thermal loads), including measurements for fine particle (PM_1) number size distribution, number concentration, and chemical composition. The experiments were complemented with Computational Fluid Dynamics (CFD) simulations and Plug-Flow Reactor (PFR) modeling. The measurements and modeling are combined in a comprehensive analysis, providing fundamental understanding on the aerosol processes inside the furnace. The wood-powder combustion is efficient under both thermal loads, indicated by the low unburned carbon content in fly-ash, and the low CO, NO and soot emissions (<0.3 mg/Nm^3). The fine particles consist mainly of K_2SO_4, and of lesser amounts of alkali salts (NaCl, KCl), and Ca and Mg compounds (oxides or sulfates). A large concentration of KOH/K_2CO_3 vapor may exist in the flue gas and play a significant role in the heat exchanger fouling. The applied modeling tools are shown to provide accurate estimations for the composition and formation regions of fine particles inside the industrial biomass furnaces.

1. Introduction

Biomass and waste are important energy sources, accounting for 10% of the world's final energy consumption [1]. Biomass is used extensively in the heat and power generation, and has an important role in the climate change mitigation scenarios [2]. Biomass can replace coal in the existing power plants, and serve as a fast-track solution to decrease our fossil fuel dependency [3]. New biomass combusting heat and power plants are being constructed around the world. In the Nordic countries Finland and Sweden, biomass accounts for approximately 20% of the final energy consumption. In both countries, biomass combusting district heating plants produce a large share of the total heat supply, and new plants are being built in many regions. In IEA net zero projections, biomass combustion may account for 50% of the global district heat demand in 2050 [4].

Many technological and environmental challenges in biomass combustion are related to the particulate emissions. In incomplete combustion, the hydrocarbons released from biomass devolatilization may form soot particles, which induce a strong radiative climate forcing if released to the atmosphere [5]. The light-absorbing fraction of particles, referred to as soot, Black Carbon (BC) or Elemental Carbon (EC) depending on the measurement methodology, is estimated to have the second strongest warming impact on the climate after carbon dioxide emissions [6]. The formation of soot has been extensively studied in laboratory flames with simple gaseous hydrocarbon fuels [7–9]. The formation occurs through nucleation of gaseous hydrocarbon precursors, followed by surface growth and particle coagulation. Oxidation may remove the already formed soot if the combustion technology is appropriately designed. These subprocesses are typically included in the mathematical models of soot formation. The models are applied for example in Computational Fluid Dynamics (CFD) simulations, which

* Corresponding author.
E-mail address: niko.niemela@tuni.fi (N.P. Niemelä).

https://doi.org/10.1016/j.combustflame.2021.111960

are used in the research and development of combustion devices, such as the internal combustion engines [10,11]. In biomass combustion, the soot formation is a complicated physicochemical process, because a wide variety of hydrocarbon gasses and tars are involved. The soot formation strongly depends on the combustion conditions and the chemical properties of the biomass [12].

In addition to soot, various other aerosol particles are formed in combustion, mainly from the inorganic ash elements within the biomass. Some aerosols, such as sulfates, have a negative radiative climate forcing [5], and in contrast to soot have a cooling effect on the climate. Some ash elements induce technological challenges in the combustion applications, such as slagging, fouling, and corrosion of the heat transfer surfaces. The main problematic elements are potassium (K), sodium (Na) and chlorine (Cl) which can vaporize from the biomass and form alkali salts in the flue gas [13]. The salt vapors may directly condense on the cold heat transfer surfaces. Alternatively, they can nucleate into submicron (PM_1) particles which gradually grow larger by condensation and coagulation, and may deposit on the surfaces through thermophoresis and other mechanisms [14]. The KCl and NaCl salts are especially problematic, because they can form sticky and corrosive deposit layers whereon the coarse fly-ash particles further adhere. These deposits are hard to remove by the soot-blowing machinery. If the fuel contains enough sulfur, the chlorides may also react into less problematic alkali sulfates (K_2SO_4/Na_2SO_4). As such, sulfur containing additives can be used for reducing the alkali chloride related issues [15].

The alkali aerosols are formed through complex physical and chemical routes. The ash elements are partially vaporized during the biomass devolatilization and char oxidation stages, but may also remain in the coarse fly-ash depending on the biomass properties [16–18]. Evaporation of the elements depends on many factors, such as the fuel particle size, combustion temperature, heating rate, and molar ratio between the different elements (such as K/Si). The aerosol formation has been extensively studied in small scale experiments, and reaction mechanisms have been developed to understand the precursor chemistry in the gas-phase [19,20]. In large scale biomass combustion, studies have been conducted for fluidized bed boilers [21–24] and grate furnaces [25–27], but less information exists for pulverized fuel (suspension firing) technology.

As described above, understanding the formation of soot and inorganic aerosols is important in terms of many environmental and technological aspects of biomass combustion. The scientific fundamentals of these processes are relatively well understood in small-scale laboratory environment, but less studied in the power plant scale. In this work, the soot and fine particle formation is examined in a modern pulverized wood-burning 100 MW_{th} district heating plant. The aerosol concentrations and chemical compositions were measured for two thermal loads (30% and 100%) at two locations inside the furnace. The aerosol was characterized by online measurements for the particle number concentration, particle number size distribution, and BC concentration. Offline samples were collected using low pressure impactors, from which the elemental carbon (EC), organic carbon (OC), and water-soluble ions (K, Cl, Na, SO_4, Ca, Mg) were analyzed. In addition, several modeling tools are applied in this work for explaining the experimental findings and for gaining more detailed insight on the aerosol formation fundamentals. A CFD model of the heating plant is used for combustion simulations, and interactions between the biomass particles, gas-phase chemistry, and soot formation are studied. The CFD model results are used together with a Plug-Flow Reactor (PFR) model to characterize the chemistry of K-Cl-S species inside the furnace. Based on the combination of measurements and modeling, a comprehensive analysis for the in-furnace aerosol phenomena is presented. The introduced modeling tools can be used for solving the aerosol-related problems in pulverized biomass combustion applications.

Table 1
Proximate and ultimate analysis for the wood pellets burned as a mixture in the heating plant.

	Wood pellet 1	Wood pellet 2
	Proximate analysis	
Moisture (m-%, ar)	6.6	6.9
Volatiles (m-%, db)	84.1	85.1
Char, by diff. (m-%, db)	15.0	14.5
Ash, 550 °C (m-%, db)	0.9	0.4
LHV (MJ/kg, db)	18.58	19.08
	Ultimate analysis (dry basis)	
C (m-%)	50.1	50.9
H (m-%)	5.9	6.0
O (m-%), by diff.	43.7	42.9
N (m-%)	0.24	0.17
S (mg/kg)	150	60
K (mg/kg)	1000	410
Na (mg/kg)	57	53
Cl (mg/kg)	50	20
Ca (mg/kg)	2500	790
Mg (mg/kg)	250	140
Si (mg/kg)	350	31
P (mg/kg)	150	34

2. Materials and methods

Fig. 1 presents an overview of the research conducted in this paper. The main goal is to provide fundamental understanding on the combustion process in a modern 100 MW_{th} pulverized wood heating plant, focusing on the soot and aerosol formation. Experimental data was collected from the plant under two thermal loads (100% and 30%) in different measurement locations. The measurements are complemented with extensive modeling, providing understanding on the interactions between the fuel particles, gas-phase chemistry, soot formation, and sub-micron (PM_1) aerosol processes. The following subsections provide a detailed description of the measurements and modeling included in this work.

2.1. Experimental

Fuel properties

A mixture of two slightly different wood pellets was burned in the heating plant during the measurement campaign. The ultimate and proximate analysis for both fuels is presented in Table 1. The pellets have very similar properties, the most significant differences being the higher heating value, and the slightly lower ash and nitrogen content of pellet 2. The trace element concentrations are rather similar as well. The most important elements for fine particle formation (K/Cl/S/Na) exist in similar ratios, the potassium content being much higher compared to the others. The low chlorine content in both pellets is favorable, as it decreases the risk for chlorine related corrosion in the heat transfer surfaces. The exact combustion ratio of the pellets during the measurement campaign is not known, and a 50/50 ratio is used in most calculations of this work. For the relevant results, error limits are presented for different mixing ratios.

Sample collection with high temperature probe and dilution with eDiluter

The instruments used in the heating plant measurement campaign are presented in Fig. 2. The samples were collected from the furnace using a high temperature probe (HT-probe). The HT-probe was introduced for the first time in Ref. [28], where sulfate additive effects on the fine particles were studied in a pilot-scale flu-

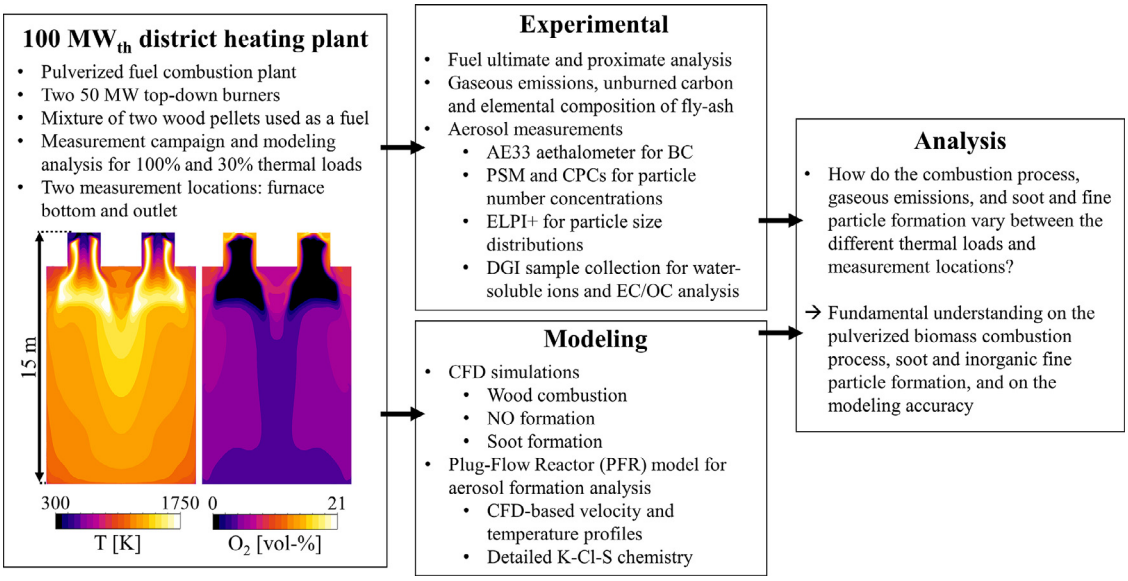

Fig. 1. Overview of the research presented in this paper.

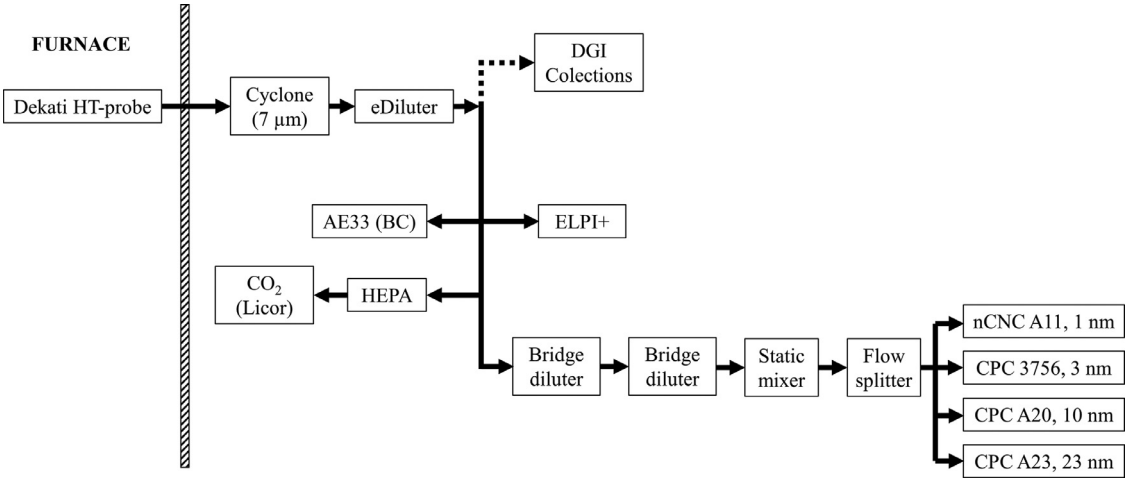

Fig. 2. Schematics of the aerosol measurement set up used in the measurements from the bottom of the boiler and empty pass of the boiler.

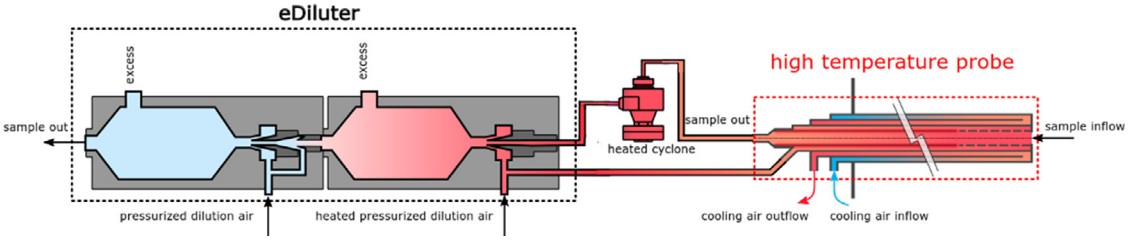

Fig. 3. Operation principle of the eDiluter and high temperature probe. Flow direction from right to left.

idized bed reactor. Later, the probe has been used for studying the particle composition in circulating fluidized bed boiler [29], pulverized coal-fired boiler [30], and bubbling fluidized bed boiler [15]. Commercial version of the HT-probe (Dekati Ltd.) was used in this study. Detailed information on the probe can be found from Refs. [31,32]. Briefly, the HT-probe dilutes the aerosol with a permeable tube diluter located at the tip of the probe (see Fig. 3). The dilution air temperature can be adjusted up to 400 °C and the sample cools down in the dilution according to the sample and dilution air flow rates and temperatures. The dilution air creates a sheath flow around the aerosol sample, preventing vapor and particle losses to the walls. Cooling air runs in a mantle enveloping the probe and protects it under the harsh conditions inside the furnace.

The eDiluter Pro (Dekati Ltd., see details in Refs. [33,34]) is a two-stage sheath flow ejector diluter, where the dilution stages are a combination of an axial diluter and an ejector diluter (see Fig. 3). An essential feature of the eDiluter Pro is the constant Dilution Ratio (DR) independently of the inlet pressure variations in the sample flow. This is done by measuring the sample pressure and actively controlling the dilution air pressure to compensate the ef-

fects of pressure variations. This is due to the fact that the aerosol reaches the critical velocity in the eDiluter's ejector which in turn stabilizes the volumetric aerosol sample flow rate, and also enables the possibility to compensate the changes in DR by adjusting the dilution air pressure.

The HT-probe and the eDiluter are connected in a way that the eDiluter's first axial diluter is replaced by the HT-probe's permeable tube diluter, and the sample outflow from the probe is maintained by the ejector of the first dilution stage. The air in the first dilution stage was heated to 400 °C. After the HT-probe, a heated cyclone (400 °C) was used to remove the coarse fly-ash particles from the sample. In this work, the total DR was kept at 225 in all measurements. As shown by the measurement setup in Fig. 2, the sample was led to the various aerosol instruments after the eDiluter-unit.

Online aerosol instruments and offline analyzation techniques

Particle number concentration was measured continuously by several instruments with different cut-points for the particle diameter. Airmodus A11 nanoCondensation Nucleus Counter (nCNC), with the ability to count particles down to 1 nm size, was measuring in parallel with an A20 condensation particle counter (CPC) with a 10 nm cut-point, and an A23 CPC with a 23 nm cut-point. Measurement data was logged with a MultiCPC software. In addition, the particle number concentration was measured by a TSI 3756 CPC with a 2.5nm cut-point. Two bifurcated flow diluters (bridge diluters), combined with a static mixer and a flow splitter, were applied before the nCNC and CPCs to lower the particle concentration to suitable level, and to mix and equally distribute the sample.

Particle number size distributions were measured by an electrical low-pressure impactor ELPI+ [35] (Dekati Ltd.). ELPI+ charges the particles in a corona charger before classifying them based on the aerodynamic diameter in an impactor column. In impactor stages, the particles that cannot follow the flow path are impacted on a substrate (sintered plates) and the electrical current carried by the particles is measured and converted into number concentration.

Black Carbon (BC) was measured by an AE33 dual-spot aethalometer [36] (Magee Scientific) equipped with a PM_1 cyclone. In this experiment, the AE33 online compensation parameter could not be used because the filter tape collection location was changed often (about every 20–30 min). The AE33 data was corrected offline by calculating new compensation parameters as described in Appendix A.

Particle samples for offline analyses were collected by a Dekati gravimetric impactor (DGI). The DGI consists of five stages with cut-off diameters of >2.5 µm, 2.5 µm to 1 µm, 1 µm to 0.5 µm, 0.5 µm to 0.2 µm, and <0.2 µm. The smallest size fraction was collected on a quartz filter (Whatman QM-A, UK), whereas the other four impactor stages were greased (Apiezon L) polycarbonate membranes (Nuclepore, pore size 0.2 µm). The size classified DGI samples were analyzed offline with the methods described below. The results shown in this article are from the lowest three stages of DGI, i.e. corresponding to PM_1.

The inorganic ions were analyzed from the DGI samples using ion chromatography (IC). The ions were extracted by shaking the samples with 5 ml of deionized water in a test tube for 15 min. ICS-2000 ion chromatographs (Dionex, US) were used for quantifying the anions (Cl^-, SO_4^{2-}) and cations (Na^+, K^+, Mg^{2+}, Ca^{2+}) in the samples. The IC-2000 systems had AS11/CS12A/AG11/CG12A analytical/guard columns (4 mm), 500 µl loops, AERS/CERS 500 suppressors, and KOH eluent for anions and MSA eluent for cations. For all ions, the uncertainty of the IC analysis was estimated to be approximately 10–15% when the analyzed concentration was >10 ng/mL, and 15–30% when it was <10 ng/mL.

Monosaccharide anhydrides (MAs), levoglucosan, galactosan and mannosan, are water-soluble compounds formed in biomass pyrolysis. They can be used as a marker of incomplete combustion of the pyrolysis gasses. The concentration of MAs was analysed using a high-performance anion-exchange chromatography–mass spectrometry (HPAEC-MS). The analytical method is similar with the one described in Ref. [37], except that the used internal standard was methyl-β-D-arabinopyranoside. Shortly, the sugars were extracted from a 1 cm^2 filter punch using 5.0 mL of deionized water (with internal standard 100 ng mL^{-1}), and the HPAEC-MS was then utilized for measuring the levoglucosan, mannosan, and galactosan at *m/z* 161. The HPAEC-MS system had a 2 mm CarboPac™ PA10 guard and analytical columns (Dionex), potassium hydroxide (KOH) as an eluent, an EI ionization technique, and a MS quadruple mass analyzer.

Organic Carbon (OC) and Elemental Carbon (EC) samples were collected to the backup filters of the DGI and analyzed using a thermal-optical technique based on the evolution of carbon species in different temperatures (Lab OC-EC Aerosol Analyzer, Model 5, Sunset Laboratory Inc., US [38]). The thermal-optical temperature protocol used in this study was EUSAAR2 [39]. The analysis consists of three stages: first, the OC is desorbed from the filter punch (1.5 cm^2) through progressive heating under a pure He stream. However, a fraction of OC chars and forms pyrolyzed OC during that stage. In the second stage, the sample is heated under a mixture of 90% He–10% O_2, during which the pyrolyzed OC and EC are desorbed. After being vaporized, OC, EC and pyrolyzed OC are finally converted to CH_4, which is quantified with a flame ionization detector. In the third stage, an internal standard (5% CH_4 in helium) is injected into the instrument. To correct for the pyrolysis effect, the transmittance of a 658 nm laser beam through the filter media is recorded. The split point, which separates pyrolyzed OC from EC, is determined as a point where the laser signal returns to its initial value.

Gaseous NO and CO emissions of the heating plant are continuously measured from the stack by the plant operator. The data from the duration of the measurement campaign was obtained from the plant's automation system and was time-averaged for obtaining the mean emissions (and standard deviations) for further model comparison.

Unburned carbon (UBC) and elemental composition of fly-ash were analyzed from bag-house filter (BHF) ash samples with loss-on-ignition tests and X-ray fluorescence (XRF), respectively. The fly-ash samples were collected after each operating load's test campaign from two different sections of the BHF. A total of four samples for each load were analyzed for the UBC and averaged for obtaining data on the biomass char burnout efficiency. The XFR analysis (Thermo Scientific™ Niton XL3t GOLDD+) was conducted similarly for four samples and averaged for obtaining the concentration of main elements in the fly-ash. The reproducibility of the XFR device was ensured by conducting double tests for the same samples, and the results were generally very consistent.

2.2. Modeling

CFD model of the heating plant

The heating plant configuration is visualized in Fig. 4. The combustion system consists of two 50 MW burners attached on the roof of the furnace. A masonry pre-combustion chamber ensures efficient ignition for the flame. Swirling air and recirculated flue gas are fed into the burner through primary and secondary inlets, whereas tertiary nozzles provide additional staging-air. The boundary conditions for the simulations, such as the burner mass flow rates, were obtained from the plant operator. The total air-fuel equivalence ratios were 1.3 and 1.5 for the 100% and 30% operating loads, respectively. The equivalence ratios for the burner were

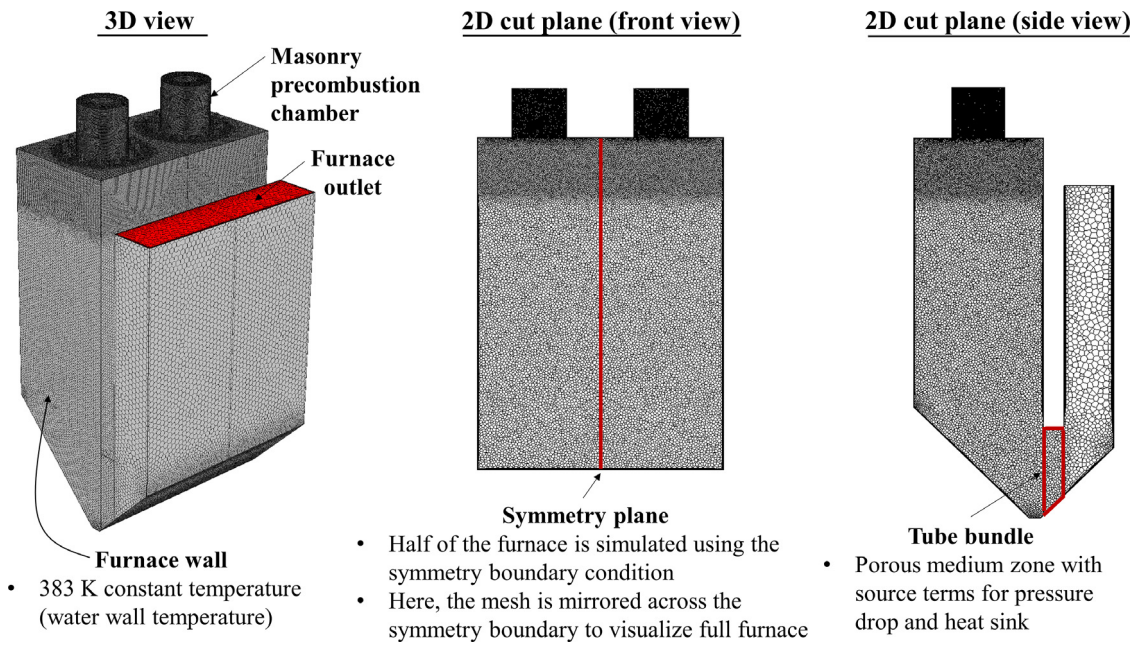

Fig. 4. 3D and 2D views of the 100 MW heating plant furnace, displaying the simulation domain, important boundary conditions, and computational mesh with 2.9 million cells.

0.6 (100% load) and 1.0 (30% load), and the remaining air was fed through the tertiary nozzles after the pre-combustion chamber. The complete furnace construction is shown in Fig. 4, but only half of the domain is included in the simulations by using symmetry boundary condition at the furnace center plane. Multiple meshes with different refinement regions were initially tested, and the shown configuration was found to provide accurate results with relatively low total cell count. The burner and flame regions are meshed with a very fine resolution, and the cell size increases towards the furnace outlet. As a mesh independence study, three simulations with 1.0, 2.9, and 6.3 million polyhedral cells were tested for the 100 MW simulation. The two finest meshes (2.9 and 6.3 million cells) provided similar results in terms of axial temperature distribution and CO and soot results, and the mesh with 2.9 million cells was used for the simulations of this work.

The CFD solution is based on the Favre-Averaged Navier-Stokes methodology, using the Realizable $k-\epsilon$ model with standard wall functions for the turbulence closure. The partial differential equations describing the fluid flow and turbulence can be found in Refs. [40,41]. Ansys Fluent R2019 software [41], which uses the Finite-Volume Method (FVM) for numerical solution, is used throughout this work. The numerical settings include the least-squares cell based method for gradient approximation, the PRESTO!-scheme for pressure discretization, and the second order upwind scheme for other variables. The pseudo-transient coupled algorithm is used for the iterative solution because of its good convergence stability. The important submodels are presented in Table 2.

Fig. 5 presents an overview of the fuel particle and gas phase subprocesses being modeled in this work. The CFD model setup and the biomass particle submodels include a great number of equations and parameters, and only a brief description is given here. A detailed model presentation is given in Ref. [43], where a validation study with 120 kW pilot reactor combustion experiments is provided. The biomass particle trajectories are calculated with the Lagrangian Discrete Phase Model (DPM). The size distribution for particle calculations is determined with an imaging software that calculates the sphere-equivalent diameters from 2D particle projections. The measured d_{50} and d_{90} diameters for the fuel powder are 330 µm and 600 µm, respectively. The particle combustion occurs in three stages: 1) moisture evaporation, 2) devolatilization, and 3) char oxidation. Equations for solving the trajectories, temperature histories, and mass transfer processes are given in Ref. [41].

Table 2
Submodels for the CFD simulations.

Feature	Submodel
Turbulence	$k-\epsilon$ Realizable, Standard wall-functions
Turbulence-chemistry interaction	Eddy Dissipation Concept (EDC)
Reaction mechanism	14 species and 9 global reactions
Fuel particle trajectories	Lagrangian Discrete Phase Model (DPM)
Fuel particle devolatilization	Single First Order Reaction (reactivity parameters from Ref. [42])
Fuel particle char oxidation	Kinetics and Diffusion Limited
Radiative heat transfer	Discrete Ordinates (DO), WSGGM for gas absorption coefficient
NOx model	Thermal (extended Zeldovich), prompt, and fuel formation paths
Soot model	Method of Moments (MoM) with HACA mechanism

The moisture evaporation is computed with the convection and diffusion-controlled method. The devolatilization is calculated with the Single First Order Reaction (SFOR) model, using reactivity parameters from high heating rate Drop-Tube Reactor (DTR) experiments. The parameters were optimized for the wood pellet 1 in Ref. [42]. The large particles ($d_p > 170$ µm) have own parameters that account for the lower devolatilization rate imposed by the internal heat transfer resistance. Furthermore, the fuel volatile content is taken from the DTR experiments (94.2 m-%) as it resembles more of the flame conditions compared to the standard proximate analysis of Table 1. The optimized devolatilization parameters ensure that the volatiles are released at the correct location inside the flame, providing accuracy for the ignition, NO_x, and soot formation predictions. After devolatilization, the residual char reacts with oxygen and forms CO and CO_2 in a 50/50 ratio. The oxidation rate is computed with the kinetics and diffusion limited

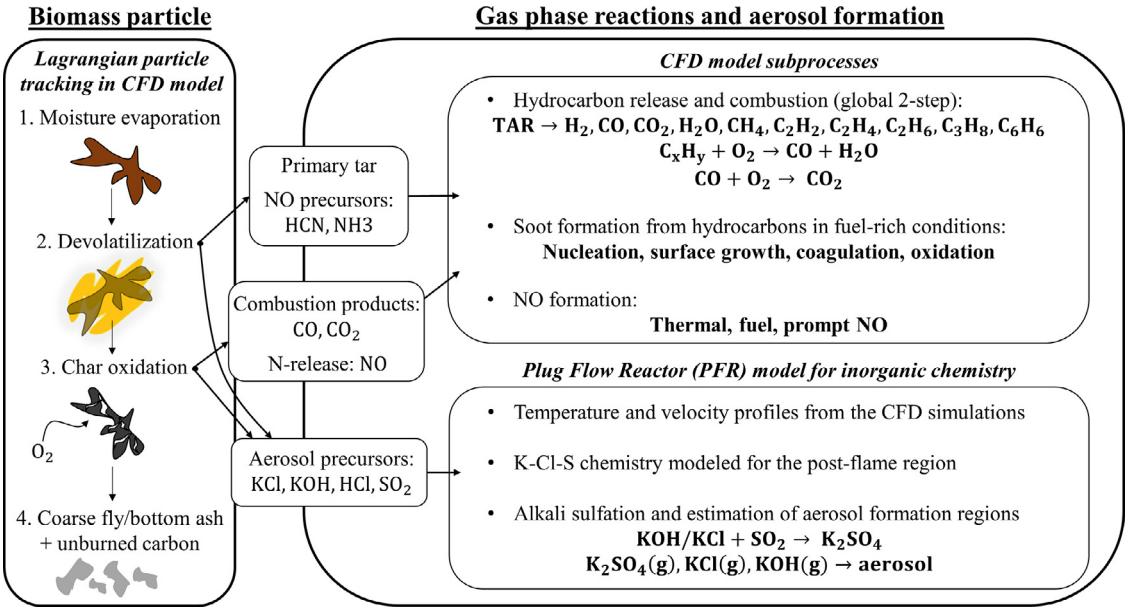

Fig. 5. Interaction of particle combustion stages, gas-phase chemistry, and aerosol formation.

Table 3
Gas-phase reaction mechanism for the CFD simulations. Reaction 1 calculated based on wood pellet 1 composition.*.

Reaction	A	E_a	β	a	b	#
$CH_{1.558}O_{0.714} \rightarrow 0.165H_2 + 0.423CO + 0.105CO_2 + 0.081H_2O + 0.090CH_4 + 0.011C_2H_2 + 0.095C_2H_4 + 0.031C_2H_6 + 0.002C_3H_8 + 0.017C_6H_6$	5.000e14	0	0	TAR : 1	–	(R1)
$H_2 + 0.5O_2 \rightarrow H_2O$	9.870e08	3.100e07	0	H_2 : 1.0	O_2 : 1.00	(R2)
$CH_4 + 1.5O_2 \rightarrow CO + 2H_2O$	5.012e11	2.000e08	0	CH_4 : 0.7	O_2 : 0.80	(R3)
$C_2H_2 + 1.5O_2 \rightarrow 2CO + H_2O$	4.390e10	1.256e08	0	C_2H_2 : 0.5	O_2 : 1.25	(R4)
$C_2H_4 + 2O_2 \rightarrow 2CO + 2H_2O$	1.350e10	1.256e08	0	C_2H_4 : 0.1	O_2 : 1.65	(R5)
$C_2H_6 + 2.5O_2 \rightarrow 2CO + 3H_2O$	7.310e09	1.256e08	0	C_2H_6 : 0.1	O_2 : 1.65	(R6)
$C_3H_8 + 3.5O_2 \rightarrow 3CO + 4H_2O$	5.620e09	1.256e08	0	C_3H_8 : 0.1	O_2 : 1.65	(R7)
$C_6H_6 + 4.5O_2 \rightarrow 6CO + 3H_2O$	1.350e09	1.256e08	0	C_6H_6 : −0.1	O_2 : 1.85	(R8)
$CO + 0.5O_2 \rightarrow CO_2$	2.239e12	1.700e08	0	CO : 1.0	O_2 : 0.25	(R9)

* Arrhenius parameters for $k = AT^{\beta}exp(-E_a/R_uT)$; rate exponents a and b; units J, kmol, K, s, m.

model, with the pre-exponential factor, activation energy, and diffusion rate constant set as 0.002 1/s, 70 kJ/mol, and 5e-12 (-), respectively. The Fluent database values for coal are used because no experimental data is available, but the activation energy is lowered from 79 to 70 kJ/mol to account for the higher reactivity of biomass chars.

As described in Fig. 5, the volatiles are released from the fuel as a primary tar. The tar decomposes rapidly into various hydrocarbons that react further in the flame. The complete gas-phase combustion mechanism is presented in Table 3. Reaction R1 describes the tar decomposition, which is followed by the global hydrocarbon combustion reactions R2-R9 according to the Westbrook and Dryer kinetics [44]. The turbulence-chemistry interaction is modeled with the Eddy Dissipation Concept (EDC) [45], which combines the turbulent mixing rate and chemical kinetics for the mean reaction rate calculation in each computational cell.

Soot formation modeling

Soot formation and growth in biomass pyrolysis, gasification and combustion may occur at least through three mechanism: 1) the CPD (cyclopentadienyl, c-C_5H_6) route related to lignin decomposition, 2) the direct condensation of aromatics in pyrolysis products, and 3) through the lighter hydrocarbons that grow by the Hydrogen Abstraction C_2H_2 Addition (HACA) mechanism [12,46,47]. Aromatic hydrocarbon ring species are crucial components in all mechanisms, as they form Polycyclic Aromatic Hydrocarbons (PAHs) which are considered the main precursors for soot nuclei in high temperatures. The oxygen-rich primary tars released at the initial stage of biomass devolatilization (200–500 °C) decompose into hydrocarbon gasses and secondary/tertiary tar species at higher temperatures [48]. In fast pyrolysis tests of Ref. [46] (sawdust and straw), the main tar components and soot precursors in temperatures above 900 °C were benzene (C_6H_6) and PAH molecules such as toluene (C_7H_8), naphthalene ($C_{10}H_8$) and pyrene ($C_{16}H_{10}$). C_6H_6 accounted for over 50 m-% of the tar species at 900 °C and over 90 m-% at 1100 °C. The CPD and direct condensation mechanisms had a minor contribution to the soot formation. As such, benzene and the lighter PAHs are likely the main soot precursors also in high temperature biomass flames (combined with HACA growth).

In this work, a global reaction mechanism is used where the primary tar decomposes directly into the main high temperature soot precursors, C_6H_6 and C_2H_2 (see R1 in Table 3). The stoichiometric coefficients for R1 are determined based on Ref. [49], where Drop-Tube Reactor experiments in various temperature levels were used for characterizing the wood devolatilization products. A global pyrolysis reaction was derived for wood decomposition into tar ($C_8H_{10}O_4$), gasses (H_2, CO, CO_2, H_2O, hydrocarbons up to C_8H_{10}), and residual char. A cracking reaction of tar into lighter hydrocarbon species was also derived. The wood in their

work had a slightly different C/H/O composition and lower volatile content than the pellets in this work, and some adjustments are made to ensure conservation with the ultimate analysis. This is done by distributing the excess volatile carbon content between the gasses according to their experimental mass fractions. Finally, the H_2 and H_2O concentrations are altered to balance the hydrogen and oxygen conservation. Furthermore, the heavier aromatic compounds (C_7H_8 and C_8H_{10}) are lumped into C_6H_6 for reducing the number of transport equations in CFD modeling. This approach provides a good starting point for soot formation modeling in pulverized biomass combustion, as a wide selection of hydrocarbons can be used as precursors and surface growth species.

Soot formation is computed with the Method of Moments (MoM) model [41], which is based on the population balance equations. Three moments are solved for obtaining the concentration, mean diameter, and surface area of the soot particles. The nucleation, surface growth, coagulation, and oxidation are accounted by source terms in the transport equations. Nucleation is modeled with the framework introduced in Ref. [50], where the nucleation rate is calculated using the collision frequency from kinetic gas theory for PAH molecules, which is scaled down by a sticking efficiency γ. For example, they use a sticking efficiency of $\gamma = 0.025$ for pyrene molecules ($C_{16}H_{10}$), but report that the efficiency decreases rapidly for smaller molecules.

Acetylene (C_2H_2) and benzene (C_6H_6) are considered as the soot precursors in this work, as they are the important building blocks of PAH molecules [51,52]. However, the sticking efficiency should be significantly lower than for the large PAHs, because it must account the overall process of PAH formation and the subsequent PAH collisions into soot nuclei. The sticking efficiency is estimated with the fourth-power equation $\gamma_i = CM_i^4$ [50], where the scaling parameter C is set to 5e-5, and M_i (kg/mol) is the precursor molecular weight. Various values for C were tested and this value was found to provide reasonable results compared to measurements from the heating plant. The resulting sticking efficiencies ($\gamma_{C_2H_2} = 2.3 \cdot 10^{-12}$ and $\gamma_{C_6H_6} = 1.9 \cdot 10^{-10}$) seem reasonably low to describe the collisional efficiency into larger PAHs and further into soot nuclei.

Soot surface growth is calculated with the HACA mechanism using kinetic rates from Ref. [53]. Rate parameters for soot oxidation by oxygen (O_2) and hydroxyl radicals (OH) are also obtained from that work. The OH radical concentration is calculated with the partial equilibrium assumption, as OH is not included in the gas-phase mechanism. Finally, the coagulation of soot particles is included in the source terms of the moment transport equations, altering the particle number concentration. The coagulation is assumed to result in spherical particles with increased diameter (coalescent growth), and depends on the collision efficiency which is calculated differently for the continuum, transition and free molecular regimes (see full description in Ref. [41]). A model for the formation of chain-like soot aggregates was also tested, but because of the low soot concentrations it did not affect the simulation results.

NO formation modeling

The NO emissions are modeled with the thermal, prompt, and fuel formation paths. The thermal NO is calculated with the extended Zeldovich mechanism with partial equilibrium assumption for O and OH radicals. The prompt NO forms in the fuel rich region from the hydrocarbon species as described in Ref. [41]. In the combustion conditions of this work, the fuel NO has the greatest contribution to the overall NO emissions. The experiments in Ref. [54] indicate that biomass fuels with low fuel-N content (<1 m-%, db) release the nitrogen effectively into gas phase. For biomass, most of the fuel-N is released during devolatilization in the form of NH_3 and HCN, whereas the char-bound nitrogen is released mainly as NO [54]. In this work, 90 m-% of the fuel-N content is released in devolatilization and the rest 10 m-% during char oxidation. A high volatile-N content is assumed because of the small particle size, and high heating rate, temperature, and volatile content of the wood pellets (94.2 m-%, db). Based on the trends in Ref. [54], the volatile-N is set as 59 m-% of NH_3, 21 m-% of HCN and 20 m-% of N_2, whereas the char-N is released as NO (90 m-%) and N_2 (10 m-%). Finally, the released nitrogen species react in the gas phase according to the HCN/NH_3/NO reaction mechanism described in Ref. [41]. The turbulent mean reaction rates are modeled with the probability density function utilizing a two-variable beta distribution for temperature and O_2 concentration. The global maximum flame temperature is used as the upper limit for temperature fluctuations, and the temperature variance is calculated with a transport equation.

Plug flow reactor model for fine particle analysis

Fine particle formation inside the furnace is examined with a Plug Flow Reactor (PFR) model. PFR model enables the use of complicated kinetic mechanisms that are computationally too heavy to be integrated into full scale CFD simulations. The PFR model assumes that the reactants are well mixed in the radial direction and the reactions proceed only in the flow direction. This is a reasonable approximation for the post-flame region where the flue gasses are already relatively well mixed. The PFR calculations provide detailed information on the aerosol precursor chemistry and are used for explaining the aerosol measurements in the results section. However, care must be taken in the interpretation of the results, as the real furnace conditions deviate from the ideal PFR assumptions. The modeling is conducted with the Ansys Chemkin 2019 R3 software using the detailed reaction mechanism for K-Cl-S chemistry available in Ref. [55]. A simplified description for the K_2SO_4 aerosol formation is added to the mechanism from Ref. [20]. It describes the homogenous nucleation and heterogenous condensation with an irreversible first-order reaction, ensuring rapid aerosol formation at temperature range between 1030 and 1130 K. This temperature interval was obtained from calculations based on detailed aerosol theory in Ref. [56], and experimental support has been provided in Ref. [19]. In this work, similar irreversible reactions for KCl and KOH condensation are added to the mechanism. The activation energies are adjusted so that rapid condensation occurs at 800 K for KCl and at 770 K for KOH, which correspond to a saturation ratio equal to 4 for the estimated flue gas concentrations.

The temperature and velocity profiles for the PFR model are taken as cross-sectional averages from the CFD simulations in the post-flame region of the furnace. As such, the calculations assume that most of the biomass devolatilization and char oxidation have occurred in the flame and have released the available aerosol precursors at the PFR inlet. The precursor inlet concentrations are estimated based on the ultimate analysis and K-Cl-S release factors taken from the literature. A 100% release efficiency is assumed for the Cl and S based on the high temperature pulverized fuel combustion tests in Ref. [16]. The release of K is more complicated but it has been shown to correlate with the fuel Cl and Si contents [16,17]. A high Cl content enhances the release of K (as KCl) already in the devolatilization stage [17]. On the contrary, a high Si content (molar K/Si < 2) bounds the potassium into silicates and keeps it retained in the coarse fly-ash [16,17]. The Si content is low for the pellets of this work (K/Si > 2), and it is assumed that 80% of the fuel K evaporates to the gas-phase. This estimation is taken from Ref. [18], where over 70% release efficiencies were measured for wood pellets. The released K-Cl-S elements are set as KOH, KCl, HCl and SO_2 at the PFR inlet [19,20]. The Cl content is assumed to be mainly in the form of KCl (80% of Cl), the rest being HCl. The excess K is included in KOH.

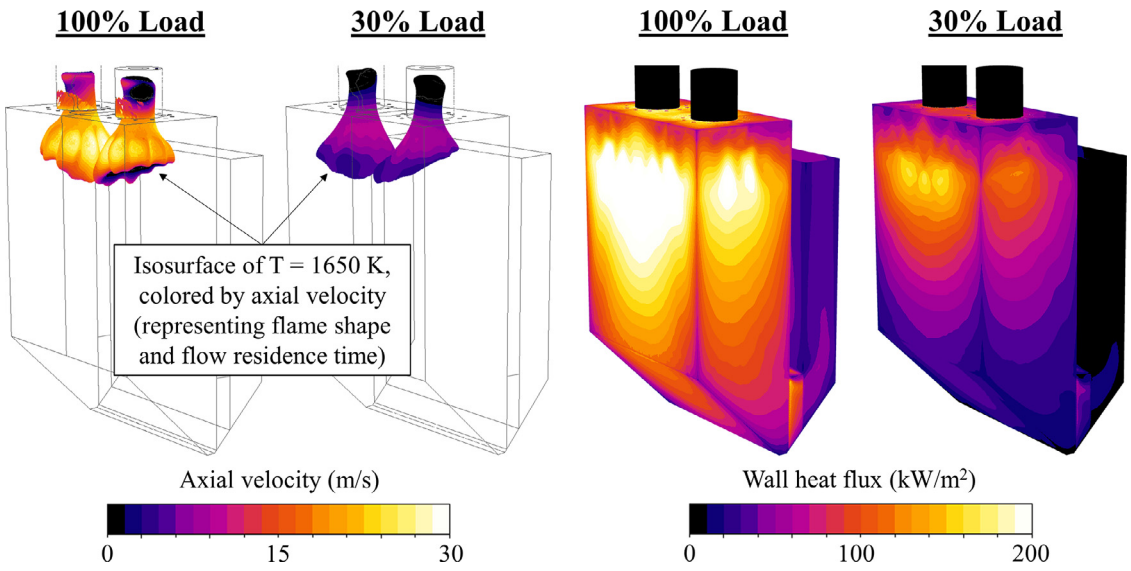

Fig. 6. Left: Isosurface of 1650 K temperature colored by axial flow velocity, representing the flame shape and gas residence time for 100% and 30% loads. Right: Heat flux through the furnace water walls.

3. Results and discussion

3.1. Formation of soot and other emissions under 30% and 100% loads

This section evaluates the biomass combustion process and emissions under the 30% and 100% thermal loads. The CFD simulation results are compared to the measured plant data, and features related to soot and fine particle formation are discussed. Fig. 6 compares the flame shape and the water wall heat fluxes between the two loads. The heat flux contours (right) demonstrate the general engineering results obtained from the CFD simulations. Fig. 6 (left) presents an isosurface of 1650 K temperature, which is colored by the axial flow velocity. The isosurface represents the flame shape inside the furnace, whereas the velocity coloring provides information on the gas and particle residence times inside the flame. The results show that the flame size is surprisingly similar for the two loads, even though the gas velocities and residence times are highly different.

Fig. 7 presents the CFD simulation results related to gaseous emissions and soot formation. Both thermal loads share similar features, such as the more intense combustion at the rear side of the furnace, and the low oxygen concentration in the flame core. The temperature in the post-flame region is significantly lower for the 30% load. This has a large impact on the fine particle formation, as will be discussed in the following section. The highest soot concentrations are found in the region where oxygen concentration is low, and the hydrocarbon concentrations are high. As Fig. 7 indicates, major concentrations of acetylene (C_2H_2) are found in this region for both loads (same applies to benzene). Despite a significant amount of soot is formed in the flame, it is effectively oxidized after mixing with the tertiary air. As such, the soot concentrations are very low at the post-flame region and furnace outlet.

The measured and CFD modeled emissions are compared in Table 4. The low CO and soot concentrations indicate that the combustion is efficient under both loads. The measured BC concentrations inside the furnace are below 0.3 mg/m^3 (<0.2 mg/MJ for both loads), which is less than measured for modern pellet stoves in residential heating (1 mg/MJ [57]) and significantly less compared to residential fire places (100–300 mg/MJ [57]). Low soot concentrations are supported by the negligible EC and OC contents detected from the filter samples (<0.01 mg/m^3). Furthermore, no monosaccharide anhydrides (MA) were detected in the measurements, indicating efficient combustion of the volatile gasses. The unburned carbon content in fly-ash (UBC) was also relatively low for both loads, which indicates that the biomass char residue burns with high efficiency. The measured UBC values are approximately 5 m-%, which means that the fuel char content has burned with over 99% efficiency. The 5 m-% UBC in fly-ash may at first seem significant, but due to the very low ash content of the wood pellets (<1 m-%), even a small amount of unburned carbon makes a large contribution to the fly-ash mass.

The emission levels predicted by the CFD model are in good agreement with the measurements, although some deviations can be noticed. Firstly, the CFD model predicts a larger difference for the NO emissions between the two loads. The difference in the modeled values is mainly caused by the different char burnout behavior in the simulations. At 30% load, the particle residence times are high, and the char is mostly oxidized in the vicinity of the flame. The NO released in the char oxidation is mixed with the NH_3/HCN that are released in devolatilization, and reduction of NO towards N_2 occurs. At 100% load, the char oxidation continues further downstream of the furnace, where volatile NH_3/HCN are no more available and less NO reduction occurs. The effect can be seen in the NO concentration fields of Fig. 7. The NO content peaks after the flame and decreases downstream at the 30% load, whereas the NO content increases all the way towards furnace outlet at the 100% load.

Compared to the measurements, the CFD model predicts larger differences for the fly-ash UBC between the two loads. Considering the low ash content of the pellets, both the experiments and simulations indicate a high char burnout efficiency (>99%). However, the measurements imply a similar UBC for both loads, so the burnout behavior is not completely realistic in the CFD model. The burnout is too efficient at 30% load, being the main reason for the low UBC and NO predictions. This is a major error source in the current CFD model, and the results could be improved by experimentally determined char oxidation parameters. In this work, the char combustion is not studied in more detail, but the results clearly imply that realistic burnout behavior is imperative for accurate UBC and NO predictions. Accurate devolatilization modeling is also important, as the largest particles continue HCN and NH_3 release in the post-flame region, and the mixing with char-NO controls the overall NO emissions. In industrial scale furnaces, the post-flame char-NO release has a relatively large impact on

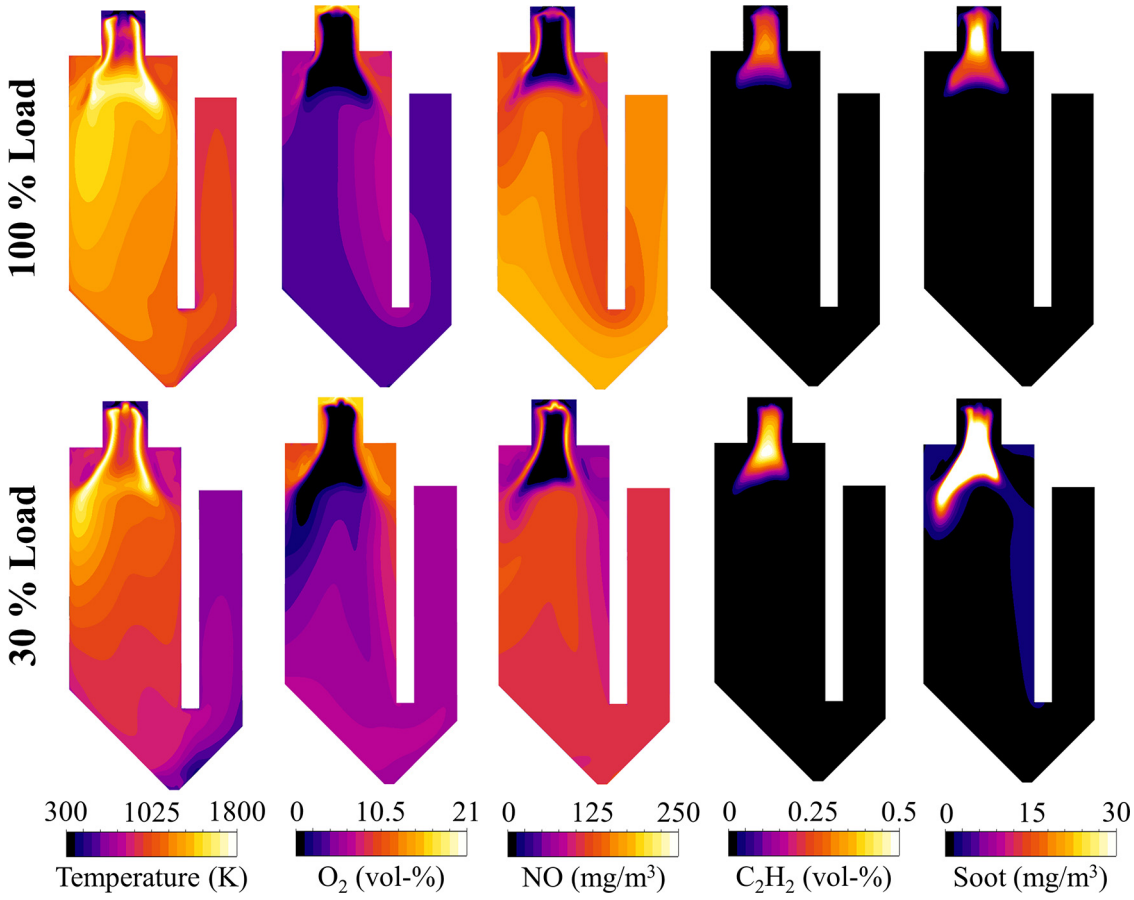

Fig. 7. Side view cut planes comparing the 30% and 100% loads in the heating plant CFD model.

Table 4
Time-averaged emissions and standard deviations from the measurement campaign. CO and NO are measured from the stack, whereas BC is measured from the furnace with the HT-probe. The UBC values are averaged over 4 bag-house filter ash samples (each load). CFD results are taken from the furnace outlet.*.

	100% Load		30% Load	
	Measured	CFD model	Measured	CFD model
CO (mg/m^3)	42.4 ± 5.9	31.2	51.5 ± 20.3	11.6
NO (mg/m^3)	157.4 ± 11.2	168.4	164.7 ± 13.1	123.6
Soot (mg/m^3)	0.27±0.02 (BC)	0.03	0.20±0.02 (BC)	1.44
UBC (m-% C in ash)	5.3 ± 0.7	11.6	4.5 ± 0.8	0.4

* Concentrations for dry flue gas at 1 bar, 288.15 K, and normalized to 6 vol-% O_2.

the NO emissions, as the flame generated NO is minimized by the efficient burners and air-staging. In future work, the char oxidation modeling should be improved especially for the low operating loads, where the flue gas temperatures can be relatively low (600–1000 K).

The soot concentration in the CFD model is slightly underpredicted for the 100% load and overpredicted for the 30% load. In larger perspective, the soot concentrations are extremely low for both loads which is well captured by the presented soot modeling approach. The major assumption in the modeling is the direct decomposition of primary tar into high temperature hydrocarbon intermediates. The temperatures in the flame core can be relatively low (<1000 K), and it is possible that more complex tar species (heavy PAHs) are present in this region. For more accurate quantitative results, it is likely that more detailed reaction mechanism with complex hydrocarbon chemistry is needed. However, it is encouraged that this simplified approach is tested in other biomass combustion applications for further validation. Considering the complexity of large-scale combustion furnaces, the presented CFD model predicts the overall soot, CO, NO and UBC levels remarkably well, although improvement e.g. in the char oxidation modeling is needed.

3.2. Fine particle formation

In this section, the fine particle formation is analyzed with a combination of measurements and modeling. The fine particle number concentrations at the furnace bottom, measured by nCNC, CPCs, and calculated from the ELPI+ data, are presented in Fig. 8. The nCNC and CPC number concentrations are shown as a function of cut-off size, i.e. the bar shows the concentration of particles larger than the indicated diameter. In case of ELPI+, the concentration represents particles between 7 nm and 1 µm. The ELPI+ measurements are in between the CPC result for >2.5 nm and

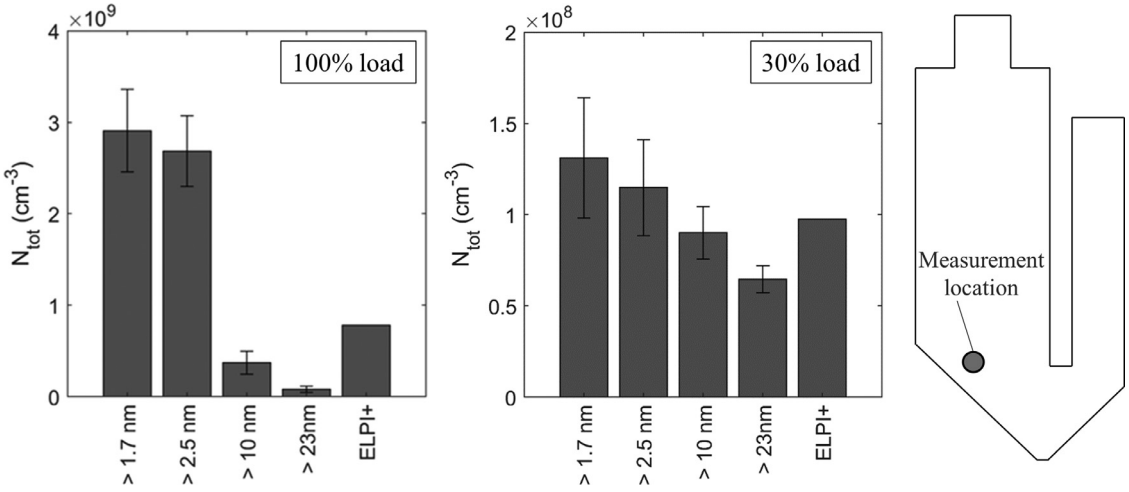

Fig. 8. Measured fine particle number concentrations at the furnace bottom. Note the different scales on y-axis.

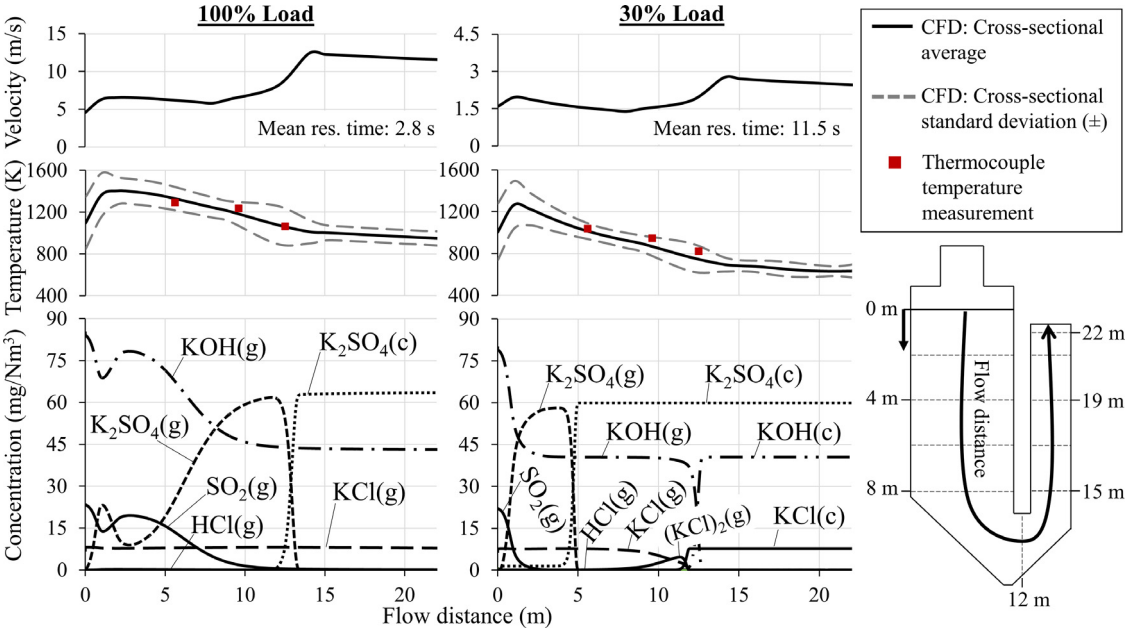

Fig. 9. Post-flame K-Cl-S chemistry calculated with plug-flow reactor model using temperature and velocity profiles from CFD simulations. Label (c) refers to condensed phase.

>10 nm, which indicates consistency between the two measurement techniques. As shown in Fig. 8, the number concentration of particles larger than 1.7 nm is 25-times higher for the 100% load as compared to the 30% load. Furthermore, the concentration of smallest particles (<10 nm; determined by subtracting $N_{>10\ nm}$ from $N_{>1.7\ nm}$) is extremely high for the 100% load, which indicates that homogenous nucleation has occurred close to the measurement location or during the sampling. In comparison, there is no indication of nucleation for the 30% load, as the total particle number is an order of magnitude lower and is largely contained in the >10 nm particle diameters (i.e. nucleation has likely occurred upstream of the measurement location and the number concentration has decreased due to particle coagulation and agglomeration).

For more detailed understanding of the measurement results, Fig. 9 presents the PFR model calculations for K-Cl-S chemistry inside the furnace. The results indicate that the SO_2 and KOH, that are released from the biomass in the flame, react effectively into potassium sulfate (K_2SO_4) in the post-flame region. The KCl concentration remains nearly constant throughout the furnace length as the high excess of KOH consumes the available SO_2. As the flue gas cools down to around 1100 K, the K_2SO_4 nucleation/condensation occurs. The KCl, on the other hand, condenses at much lower temperatures at around 800 K. It likely condenses on the existing K_2SO_4 particles and does not form new seed particles through homogenous nucleation [19,24]. The results also imply that a high amount of KOH remains in the flue gas after the sulfation reactions. This KOH likely reacts into K_2CO_3, or directly condenses on the existing particles [58–61]. According to equilibrium calculations of Refs. [58,60], K_2CO_3 formation may occur at temperatures around 900 K but the kinetics of this reaction may be slow. K_2CO_3 formation is not included in the PFR calculations and KOH is assumed to remain in the flue gas until it condenses at 770 K (i.e. close to the KCl condensation region).

Fig. 9 indicates that the aerosol formation occurs at different regions inside the furnace depending on the thermal load. At 100% load, the K_2SO_4 nucleation begins at the bottom region of the furnace. This leads to a conclusion that the high number concentration of very fine particles (<10 nm) in Fig. 8 likely results from the

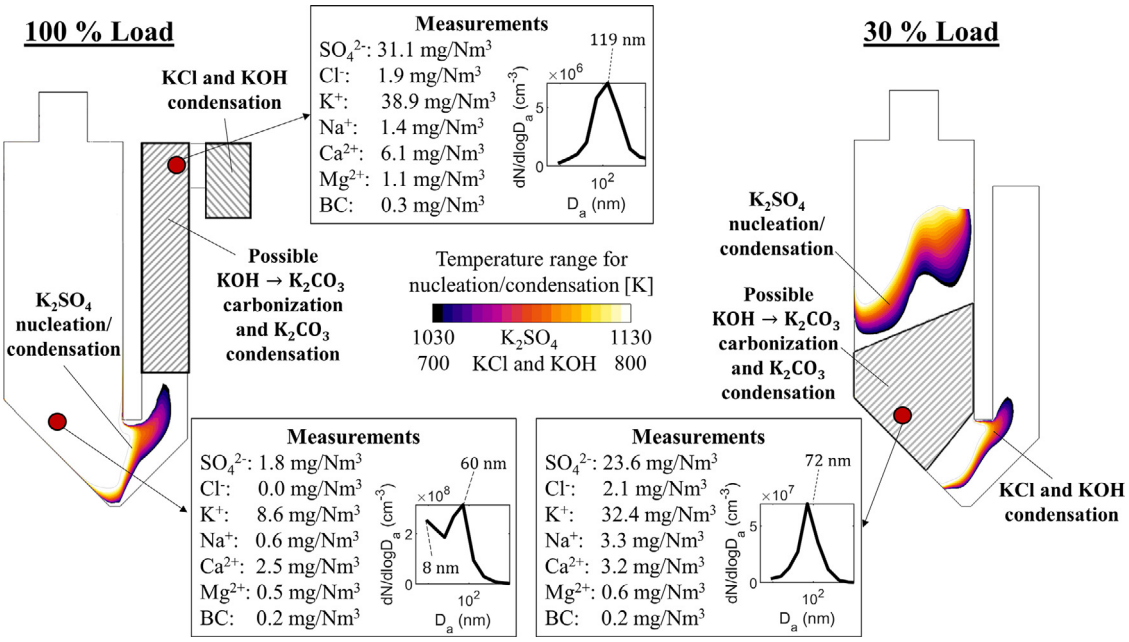

Fig. 10. Fine particle mass concentrations from IC analysis and number size distributions with median diameters from ELPI+. Measurement locations shown in the furnace layout with estimated K_2SO_4 and KCl nucleation/condensation regions.

K_2SO_4 nucleation. At 30% load, K_2SO_4 nucleation occurs already in the upper section of the furnace, which is in line with Fig. 8 where no nucleation mode particles were detected at the furnace bottom. The condensation of KCl and KOH/K_2CO_3 occurs at lower temperatures (below 900 K), which is reached in the heat exchanger region after the furnace outlet at 100% load, and in the furnace bottom region at 30% load. Some unshielded thermocouple measurements are shown in Fig. 9 for providing indication on the validity of the PFR model temperature profiles.

Experimental support for the PFR analysis is further provided in Fig. 10. It presents the Ion Cromatography (IC) results for the two loads, providing information on the chemical composition of the fine particles (PM_1). The measurement locations are shown in the embedded furnace layout together with the estimated K_2SO_4, KCl and KOH nucleation/condensation regions (based on the PFR model and CFD temperature field). The content of $K+$ cations and SO_4^{2-} anions is generally high in all collected aerosol samples. This implies that the water-soluble PM_1 largely consists of potassium sulfate, as indicated also by the PFR modeling. Moderate amounts of Ca^{2+} are also found in the samples. Compared to the high fuel Ca content (Table 1), it is evident that most of the calcium remains in the coarse fly-ash (>1 μm), but a minor fraction ends up in the fine particles. Calcium has been found in the fine particles also in circulating fluidized bed combustion of wood [24]. It might play an important role in the initial aerosol nuclei formation whereon the subsequent vapor species condense. Cl^- anions and Mg^{2+}/Na^+ cations are measured in lower amounts. The Cl content is likely in the form of alkali chlorides (KCl/NaCl), whereas the Ca and Mg likely exist in the form of oxides (CaO [24] and MgO) or sulfates ($CaSO_4$/$MgSO_4$). The BC content is very low in all measurement locations.

The particle number size distributions from ELPI+ are presented in Fig. 10 for each load and measurement location. A bimodal size distribution is clearly seen in the 100% load furnace bottom graph. The first mode median diameter is 8 nm, which is consistent with the high concentration of nucleating particles in Fig. 8. These particles were attributed to the homogenous nucleation of K_2SO_4 based on the PFR calculations. The homogenous nucleation has likely occurred during the sampling process (in the probe and cyclone, see Fig. 2) because of the extremely high saturation ratio of ≫1000 for K_2SO_4. The K_2SO_4, KCl and KOH were all vapors prior to sampling at this location, and the results indicate that they mostly condensed on the coarse fly-ash particles or wall surfaces in the probe and cyclone (thus they are not detected in the PM_1 IC analysis of DGI samples). The second particle mode at 60 nm diameter likely originates from the coagulation and agglomeration of other measured compounds (Ca, Mg, Na, BC) and non-water soluble elements (such as P, Al, Si, Zn). These particles have likely grown also by the K_2SO_4/KOH condensation in the sampling. The furnace outlet measurement (100% load) shows that the size distribution has evolved unimodal (119 nm median diameter) and the mass concentration of K and SO_4 ions has increased by a factor of 7. These features are well explained by the estimated K_2SO_4 nucleation/condensation region shown in the furnace layout, which implies that the fine particles had formed well before the measurement location (the fine particles are able to escape the cyclone and are detected in the PM_1 IC analysis).

The 30% load results in Fig. 10 demonstrate that the K_2SO_4 nucleation occurs already in the upper section of the furnace due to lower temperature and longer residence time of the flue gas. The furnace bottom measurements are in line with this observation. The size distribution is unimodal with a median diameter of 72 nm (no nucleation mode), and high concentrations of K and SO_4 ions are detected in the IC analysis. Overall, the results are line with the previous findings that the majority of initial fine particle mass is formed by nucleation/condensation of K_2SO_4, and KCl and other compounds condense on these particles [19,24]. Furthermore, it is evident that some KOH and/or K_2CO_3 has condensed on the fine particles in all measurement locations, because the K ion concentrations are higher than expected for pure K_2SO_4 and KCl.

Mass balance estimations for the main fine particle species are presented in Fig. 11. In graph a), the measurements at the furnace exit are compared to the PFR calculation (100% load in Fig. 9). The KCl and KOH were still vapors prior to sampling, which complicates the mass balance evaluation. Only the vapor mass that nucleates or condenses on the existing fine particles is detected in the IC analysis as the rest is lost into the probe and cyclone. Therefore

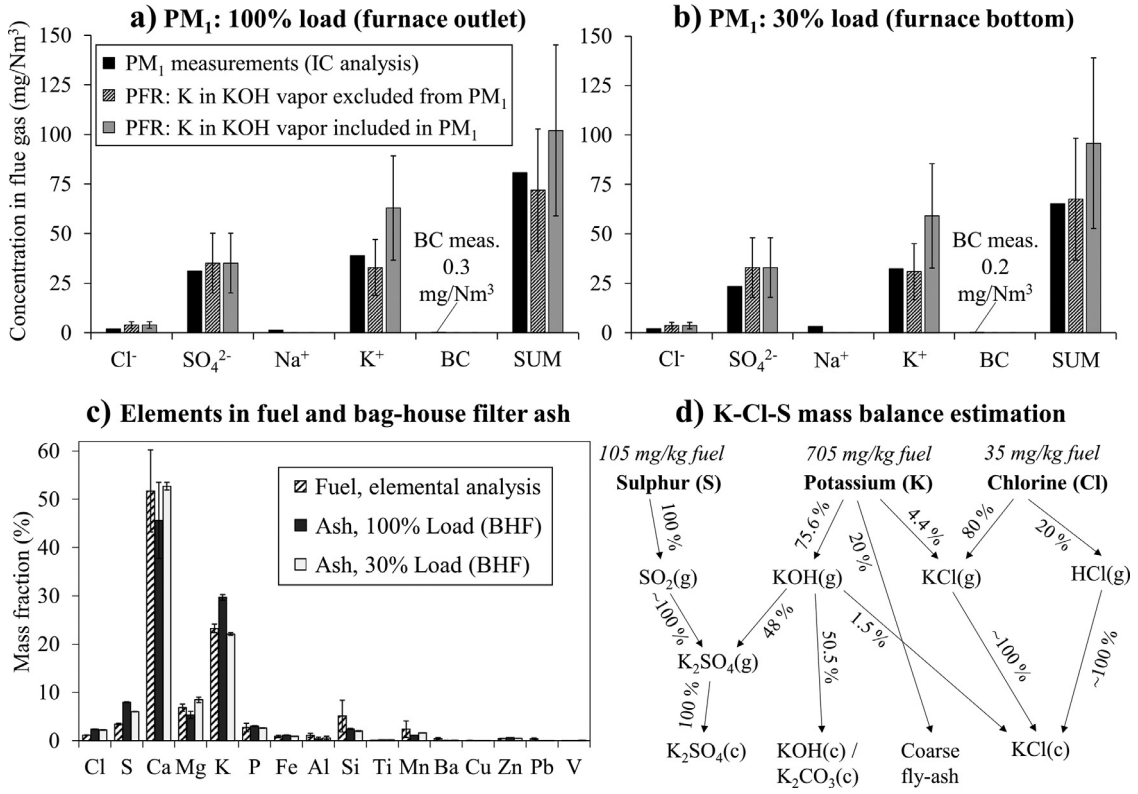

Fig. 11. a) and b) IC analysis results compared to PFR model calculations. Error bars present the lower and upper limit depending on the mixing ratio of the two wood pellets (see Table 1). c) XRF analysis for BHF ash samples (average and standard deviation of 4 samples). Results compared to elemental analysis of raw fuel. d) K-Cl-S mass balance estimation based on the measurement and modeling results.

two calculation results are shown: 1) the KOH vapor is assumed to condense on the fine particles in the sampling, and 2) the KOH vapor is excluded from the fine particle mass (i.e. it is lost in sampling). Assumption 2 is closer to the measurements, and the same applies to the 30% load case in Fig. 11 b). The real behavior of the vapor is likely somewhere between the two assumptions. In both graphs, the KCl vapor is included into PM_1 due to its low concentration, but the measurements indicate that it is also partially lost in the sampling. Overall, Fig. 11 a) and b) demonstrate that the calculation methods are accurate in this work, and are able to provide detailed estimations for the inorganic species. However, two major questions remain that cannot be deduced from the available data. Firstly, the amount of KOH vapor may not be as large as indicated by the PFR calculation, as part of the fuel-K might not have evaporated from the biomass in the first place (in which case no KOH had formed). Secondly, the degree of KOH carbonization into K_2CO_3 is unclear and needs further research.

In order to have a more complete picture on the mass balances and behavior of the inorganic species in the heat exchanger region after the furnace, ash samples from the BHF were analyzed using XRF. The results are shown in Fig. 11 c) and compared to the elemental composition of the raw fuel. The results indicate that the 30% load BHF ash has nearly identical composition with original fuel. This means that the fine particles (rich in K and S) and coarse fly-ash (rich in Ca and Mg) are not deposited in the heat exchangers, so they arrive to the BHF in unaltered ratio. The 100% load BHF ash is enriched with K and S but has lower Ca and Mg content. This indicates that some Ca-rich coarse fly-ash had deposited, whereas the K_2SO_4 fine particles had effectively passed the heat exchangers. The KOH/K_2CO_3 vapor might play an important role in this deposition, as it condenses in the heat transfer region at the 100% load and might enhance the deposition of coarse fly-ash particles (by forming a sticky layer on the pipes/ash particles [62]). At 30% load, the KOH had already condensed well before the heat transfer region, so it passed the heat exchangers without significant deposition (in the form of fine particles). Therefore, coarse fly-ash was not deposited either as a sticky condensation layer was not formed. A significant role of KOH in the heat exchanger fouling has been discussed also in Refs. [60,61,63], but the different deposition behavior between the loads in this work can be affected also by other factors (such as different flow velocities). The role of KOH/K_2CO_3 is identified as an important topic for future research.

The mass balance results are summarized in Fig. 11 d), which shows how the fuel bound K, Cl, and S elements evolve towards the fine particles. The highest uncertainty is related to the potassium division between KOH(g) and coarse fly-ash which was based on a literature estimation. Overall, the results provide confidence towards the measurement and modeling techniques adapted in this work. The CFD and PFR calculations are shown to provide an accurate estimation of the fine particle concentration, chemical composition, and formation regions in pulverized fuel combustion. This kind of fundamental understanding is valuable for solving the challenges related to inorganic species in thermochemical conversion processes. For example, the modeling can aid to design efficient additive injection systems for the industrial furnaces under different loads.

4. Conclusions and future work

Understanding the formation of soot and inorganic aerosols is important for both environmental and technological aspects of biomass combustion. The scientific fundamentals are relatively well understood in small scale laboratory environments, but less

studied in the full-scale power plants. In this work, the aerosol processes were examined in a modern pulverized wood-burning 100 MW_{th} district heating plant. The wood combustion was found to be highly efficient under both 30% and 100% operating loads. Markers for the efficient combustion were the low CO, soot, OC, and MA concentrations in the flue gas, as well as the low UBC content in fly-ash.

The flue-gas sampling, dilution, and measurements were performed with the state-of-the-art instrumentation from two locations inside the furnace. This enabled us to characterize the evolution of aerosol mass and number concentrations along the furnace. The water-soluble fine particles (PM_1) were shown to mostly consist of inorganic compounds which had nucleated/condensed from the gas phase. The main aerosol species was potassium sulfate K_2SO_4, but lower concentrations of other sulfates such as Na_2SO_4, $CaSO_4$ (or CaO), $MgSO_4$ (or MgO), and alkali chlorides (NaCl, KCl) were also measured.

The measurements were complemented with CFD simulations and PFR modeling. Soot formation was coupled to the CFD simulations with a combination of fuel-specific devolatilization parameters, global gas-phase chemistry, and MOM-model for soot subprocesses. The results were in good agreement with the BC measurements for both operating loads. The results implied that high soot concentrations formed in the fuel rich region inside the flame, but low concentrations remained at the furnace outlet due to efficient oxidation (measured BC $<$0.3 mg/Nm^3). However, the soot modeling was based on a global reaction mechanism where the primary tar decomposed directly into high temperature hydrocarbon intermediates. Detailed PAH chemistry was not simulated, but acetylene and benzene were used as the soot precursors. The sticking efficiencies for nucleation required some adjustment for realistic results, and further validation in other biomass combustion applications is needed. The presented soot modeling approach should therefore be considered as a preliminary step for more detailed studies.

The PFR model was used for studying the inorganic aerosol formation inside the furnace. The modeling provided detailed insight on the K-Cl-S chemistry and enabled identifying the nucleation/condensation regions of the different species. The results provided strong evidence that most of the biomass K-Cl-S content evaporates and forms fine particles in the suspension firing conditions. The initial seed particles are formed through homogenous nucleation of K_2SO_4 below 1130 K temperatures, and the subsequent species condense on their surface. The results implied that a high concentration of excess KOH remains in the flue gas, but its behavior could not be completely deduced from the available data. It may react into K_2CO_3 or remain in the gas-phase until condensation below 800 K temperatures. Based on the BHF ash analysis, the KOH/K_2CO_3 vapor may play a significant role in the heat exchanger fouling. As such, the KOH behavior was identified as major topic for future research.

Overall, the results provided important fundamental understanding on how the aerosol concentration, chemical composition, and size distribution vary inside the pulverized fuel furnaces under different operating loads. As the PFR calculations are performed with the detailed kinetic mechanism, the calculation methods should be valid for a variety of different fuels and combustion conditions. The kinetic mechanism also avoids misleading results that can be obtained from equilibrium calculations (due to kinetic limitations). The CFD modeling methods are applicable for other biomass furnaces and can help in the characterization of combustion performance in terms of gaseous and particulate emissions. In future work, a similar analysis can be performed for the challenging low-grade biomass feedstocks such as agricultural and industrial side streams, e.g. for solving the issues related to combustibility, emissions, and slagging and fouling.

Declaration of Competing Interest

The authors declare that they have no known competing financial interests or personal relationships that could have appeared to influence the work reported in this paper

Acknowledgements

Teemu Lepistö, Paavo Heikkilä, Laura Salo, Lassi Markkula, and Panu Karjalainen are acknowledged for the valuable help in the measurement campaign. Joni Rantanen is acknowledged for his important support in the modeling work. Fanni Mylläri is thankful for the personal and project funding provided by the Nessling Foundation. Niko Niemelä is thankful to Thorben de Riese for the fruitful discussions related to ash chemistry. The BC Footprint project (grant no. 49402–201040) funded by Business Finland, HSY, City of Tampere, and several Finnish companies, as well as the Academy of Finland flagship funding from Atmosphere and Climate Competence Center, ACCC (grant no. 337551, 337552) are gratefully acknowledged. The authors are thankful to Helen Oy and Valmet Oyj for providing the essential process and measurement data for the research.

Supplementary materials

Supplementary material associated with this article can be found, in the online version, at doi:10.1016/j.combustflame.2021.111960.

References

[1] IEA, Key world energy statistics 2020, Int Energy Agency 33 (2020) 4649.
[2] V. Daioglou, J.C. Doelman, B. Wicke, A. Faaij, D.P. van Vuuren, Integrated assessment of biomass supply and demand in climate change mitigation scenarios, Glob Environ Chang 54 (2019) 88–101, doi:10.1016/j.gloenvcha.2018.11.012.
[3] M.S. Roni, S. Chowdhury, S. Mamun, M. Marufuzzaman, W. Lein, S. Johnson, Biomass co-firing technology with policies, challenges, and opportunities: a global review, Renew Sustain Energy Rev 78 (2017) 1089–1101, doi:10.1016/j.rser.2017.05.023.
[4] International Energy Agency (IEA). Net Zero by 2050, A Roadmap for the Global Energy Sector. 2021.
[5] G. Myhre, D. Shindell, F.-.M. Bréon, W. Collins, J. Fuglestvedt, J. Huang, et al., Anthropogenic and Natural Radiative Forcing, Climate Change 2013: The Physical Science Basis. Contribution of Working Group I to the Fifth Assessment Report of the Intergovernmental Panel on Climate Change, 2013.
[6] V. Ramanathan, G. Carmichael, Global and regional climate changes due to black carbon, Nat Geosci 1 (2008) 221–227, doi:10.1038/ngeo156.
[7] T. Li, T. Mitra, C. Chu, Y. Yuan, M.J. Thomson, Investigation of PAH and soot formation in a dimethyl ether (DME) laminar coflow diffusion flame, Combust Flame 223 (2021) 437–449, doi:10.1016/j.combustflame.2020.10.019.
[8] M.D. Smooke, M.B. Long, B.C. Connelly, M.B. Colket, R.J. Hall, Soot formation in laminar diffusion flames, Combust Flame 143 (2005) 613–628, doi:10.1016/j.combustflame.2005.08.028.
[9] C. Lou, Z. Li, Y. Zhang, B.M. Kumfer, Soot formation characteristics in laminar coflow flames with application to oxy-combustion, Combust Flame 227 (2021) 371–383, doi:10.1016/j.combustflame.2021.01.018.
[10] K.M. Pang, N. Karvounis, J.H. Walther, J. Schramm, Numerical investigation of soot formation and oxidation processes under large two-stroke marine diesel engine-like conditions using integrated CFD-chemical kinetics, Appl Energy 169 (2016) 874–887, doi:10.1016/j.apenergy.2016.02.081.
[11] S. Hong, M. Wooldridge, H. Im, D. Assanis, H. Pitsch, Development and application of a comprehensive soot model for 3D CFD reacting flow studies in a diesel engine, Combust Flame 143 (2005) 11–26, doi:10.1016/j.combustflame.2005.04.007.
[12] E.M. Fitzpatrick, J.M. Jones, M. Pourkashanian, A.B. Ross, A. Williams, K.D. Bartle, Mechanistic aspects of soot formation from the combustion of pine wood, Energy Fuels 22 (2008) 3771–3778, doi:10.1021/ef800456k.
[13] J. Capablo, Formation of alkali salt deposits in biomass combustion, Fuel Process Technol 153 (2016) 58–73, doi:10.1016/j.fuproc.2016.07.025.
[14] Y. Cai, K. Tay, Z. Zheng, W. Yang, H. Wang, G. Zeng, et al., Modeling of ash formation and deposition processes in coal and biomass fired boilers: a comprehensive review, Appl Energy 230 (2018) 1447–1544, doi:10.1016/j.apenergy.2018.08.084.
[15] H. Kuuluvainen, P. Karjalainen, C.J.E. Bajamundi, J. Maunula, P. Vainikka, J. Roppo, et al., Physical properties of aerosol particles measured from a bubbling fluidized bed boiler, Fuel 139 (2015) 144–153, doi:10.1016/j.fuel.2014.08.048.

[16] A.J. Damoe, P.A. Jensen, F.J. Frandsen, H. Wu, P. Glarborg, Fly ash formation during suspension firing of biomass: effects of residence time and fuel type, Energy Fuels 31 (2017) 555–570, doi:10.1021/acs.energyfuels.6b02051.

[17] J.N. Knudsen, P.A. Jensen, K. Dam-Johansen, Transformation and release to the gas phase of Cl, K, and S during combustion of annual biomass, Energy Fuels 18 (2004) 1385–1399, doi:10.1021/ef049944q.

[18] P.E. Mason, L.I. Darvell, J.M. Jones, A. Williams, Observations on the release of gas-phase potassium during the combustion of single particles of biomass, Fuel 182 (2016) 110–117, doi:10.1016/j.fuel.2016.05.077.

[19] B. Li, Z. Sun, Z. Li, M. Aldén, J.G. Jakobsen, S. Hansen, et al., Post-flame gas-phase sulfation of potassium chloride, Combust Flame 160 (2013) 959–969, doi:10.1016/j.combustflame.2013.01.010.

[20] M.R. Mortensen, H. Hashemi, H. Wu, P. Glarborg, Modeling post-flame sulfation of KCl and KOH in bio-dust combustion with full and simplified mechanisms, Fuel 258 (2019) 116147, doi:10.1016/j.fuel.2019.116147.

[21] T. Valmari, E.I. Kauppinen, J. Kurkela, J.K. Jokiniemi, G. Sfiris, H. Revitzer, Fly ash formation and deposition during fluidized bed combustion of willow, J Aerosol Sci 29 (1998) 445–459, doi:10.1016/S0021-8502(97)10021-0.

[22] T. Valmari, T.M. Lind, E.I. Kauppinen, G. Sfiris, K. Nilsson, W. Maenhaut, Field Study on Ash Behavior during Circulating Fluidized-Bed Combustion of Biomass. 1. Ash Formation, Energy Fuels 13 (1999) 379–389, doi:10.1021/ef980085d.

[23] T. Valmari, T.M. Lind, E.I. Kauppinen, G. Sfiris, K. Nilsson, W. Maenhaut, Field Study on Ash Behavior during Circulating Fluidized-Bed Combustion of Biomass. 2. Ash Deposition and Alkali Vapor Condensation, Energy Fuels 13 (1999) 390–395, doi:10.1021/ef9800866.

[24] T. Lind, T. Valmari, E. Kauppinen, K. Nilsson, G. Sfiris, W. Maenhaut, Ash formation mechanisms during combustion of wood in circulating fluidized beds, Proc Combust Inst 28 (2000) 2287–2295, doi:10.1016/s0082-0784(00)80639-6.

[25] K.A. Christensen, H. Livbjerg, A Field Study of Submicron Particles from the Combustion of Straw, Aerosol Sci Technol 25 (1996) 185–199, doi:10.1080/02786829608965390.

[26] T. Brunner, M. Jöller, I. Obernberger, F. Frandsen, Aerosol and fly ash formation in fixed bed biomass combustion systems using woody biofuels, Proc. 12th Eur. Biomass Conf. (2002).

[27] L. Lillieblad, A. Szpila, M. Strand, J. Pagels, K. Rupar-Gadd, A. Gudmundsson, et al., Boiler operation influence on the emissions of submicrometer-sized particles and polycyclic aromatic hydrocarbons from biomass-fired grate boilers, Energy Fuels 18 (2004) 410–417, doi:10.1021/ef0300444.

[28] M. Aho, P. Vainikka, R. Taipale, P. Yrjas, Effective new chemicals to prevent corrosion due to chlorine in power plant superheaters, Fuel 87 (2008) 647–654, doi:10.1016/j.fuel.2007.05.033.

[29] P. Vainikka, J. Silvennoinen, R. Taipale, C. van Alphen, A. Moilanen, R. Falcon, et al., Halide aerosols in circulating fluidised bed co-combustion. Role of coal bound kaolin, Fuel Process Technol 92 (2011) 1738–1749, doi:10.1016/j.fuproc.2011.04.027.

[30] F. Mylläri, P. Karjalainen, R. Taipale, P. Aalto, A. Häyrinen, J. Rautiainen, et al., Physical and chemical characteristics of flue-gas particles in a large pulverized fuel-fired power plant boiler during co-combustion of coal and wood pellets, Combust Flame 176 (2017) 554–566, doi:10.1016/j.combustflame.2016.10.027.

[31] Vesala H. A diluting sampler and a method for collecting and diluting a gaseous sample. Patent: EP1974197B1, 2018.

[32] Dekati® eDiluterTM Pro 1200C 2021. www.dekati.com/products/dekati-ediluter-pro-1200c/ (accessed March 10, 2021).

[33] Niemelä V., Holma L., Lundahl S., Ukkonen A. Diluting device for aerosol measurements. Patent: FI128288B, 2020.

[34] Dekati® eDiluterTM Pro2021. https://www.dekati.com/products/ediluter-pro/ (accessed March 10, 2021).

[35] A. Järvinen, M. Aitomaa, A. Rostedt, J. Keskinen, J. Yli-Ojanperä, Calibration of the new electrical low pressure impactor (ELPI+), J Aerosol Sci 69 (2014) 150–159, doi:10.1016/j.jaerosci.2013.12.006.

[36] L. Drinovec, G. Močnik, P. Zotter, A.S.H. Prévôt, C. Ruckstuhl, E. Coz, et al., The "dual-spot" Aethalometer: an improved measurement of aerosol black carbon with real-time loading compensation, Atmos Meas Tech 8 (2015) 1965–1979, doi:10.5194/amt-8-1965-2015.

[37] K. Saarnio, K. Teinilä, M. Aurela, H. Timonen, R. Hillamo, High-performance anion-exchange chromatography–mass spectrometry method for determination of levoglucosan, mannosan, and galactosan in atmospheric fine particulate matter, Anal Bioanal Chem 398 (2010) 2253–2264, doi:10.1007/s00216-010-4151-4.

[38] M.E. Birch, R.A. Cary, Elemental carbon-based method for monitoring occupational exposures to particulate diesel exhaust, Aerosol Sci Technol 25 (1996) 221–241, doi:10.1080/02786829608965393.

[39] F. Cavalli, M. Viana, K.E. Yttri, J. Genberg, J.-P. Putaud, Toward a standardised thermal-optical protocol for measuring atmospheric organic and elemental carbon: the EUSAAR protocol, Atmos Meas Tech 3 (2010) 79–89, doi:10.5194/amt-3-79-2010.

[40] T. Poinsot, D. Veynante, Theoretical and Numerical Combustion, 2nd ed., R.T. Edwards, Inc, USA, 2005.

[41] Ansys Fluent Theory Guide, Release R2019, 33, ANSYS Inc., Canonsburg, PA, 2019.

[42] N.P. Niemelä, H. Tolvanen, T. Saarinen, A. Leppänen, T. Joronen, CFD based reactivity parameter determination for biomass particles of multiple size ranges in high heating rate devolatilization, Energy 128 (2017), doi:10.1016/j.energy.2017.04.023.

[43] N.P. Niemelä, R. Nowak Delgado, T. de Riese, H. Tolvanen, S. Fendt, H. Spliethoff, et al., Fuel-specific devolatilization parameters for detailed comparison of pulverized biomass fuels, Fuel 286 (2021), doi:10.1016/j.fuel.2020.119309.

[44] C.K. Westbrook, F.L. Dryer, Simplified Reaction Mechanisms for the Oxidation of Hydrocarbon Fuels in Flames, Combust Sci Technol 27 (1981) 31–43, doi:10.1080/00102208108946970.

[45] B.F. Magnussen, B.H. Hjertager, On mathematical models of turbulent combustion with special emphasis on soot formation and combustion, Symp Combust 16 (1977) 719–729, doi:10.1016/S0082-0784(77)80366-4.

[46] Y. Li, H. Tan, X. Wang, S. Bai, J. Mei, X. You, et al., Characteristics and mechanism of soot formation during the fast pyrolysis of biomass in an entrained flow reactor, Energy Fuels 32 (2018) 11477–11488, doi:10.1021/acs.energyfuels.8b00752.

[47] E.M. Fitzpatrick, K.D. Bartle, M.L. Kubacki, J.M. Jones, M. Pourkashanian, A.B. Ross, et al., The mechanism of the formation of soot and other pollutants during the co-firing of coal and pine wood in a fixed bed combustor, Fuel 88 (2009) 2409–2417, doi:10.1016/j.fuel.2009.02.037.

[48] R.J. Evans, T.A. Milne, Molecular characterization of the pyrolysis of biomass, Energy Fuels 1 (1987) 123–137, doi:10.1021/ef00002a001.

[49] C. Guizani, S. Valin, J. Billaud, M. Peyrot, S. Salvador, Biomass fast pyrolysis in a drop tube reactor for bio oil production: experiments and modeling, Fuel 207 (2017) 71–84, doi:10.1016/j.fuel.2017.06.068.

[50] G. Blanquart, H. Pitsch, *A Joint Volume-Surface-Hydrogen Multi-Variate Model for Soot Formation*, KIT Scientific Publishing, Karlsruhe, Germany, 2009.

[51] H. Böhm, H. Jander, D. Tanke, PAH growth and soot formation in the pyrolysis of acetylene and benzene at high temperatures and pressures: modeling and experiment, Symp Combust 27 (1998) 1605–1612, doi:10.1016/S0082-0784(98)80570-5.

[52] K. Gleason, F. Carbone, A.J. Sumner, B.D. Drollette, D.L. Plata, A. Gomez, Small aromatic hydrocarbons control the onset of soot nucleation, Combust Flame 223 (2021) 398–406, doi:10.1016/j.combustflame.2020.08.029.

[53] J. Appel, H. Bockhorn, M. Frenklach, Kinetic modeling of soot formation with detailed chemistry and physics: laminar premixed flames of C2 hydrocarbons, Combust Flame 121 (2000) 122–136, doi:10.1016/S0010-2180(99)00135-2.

[54] G. Stubenberger, R. Scharlerab, S. Zahirović, I. Obernberger, Experimental investigation of nitrogen species release from different solid biomass fuels as a basis for release models, Fuel 87 (2008) 793–806, doi:10.1016/j.fuel.2007.05.034.

[55] W. Weng, Z. Li, H. Wu, M. Aldén, P. Glarborg, Quantitative K-Cl-S chemistry in thermochemical conversion processes using in situ optical diagnostics, Proc Combust Inst 38 (2021) 5219–5227, doi:10.1016/j.proci.2020.05.058.

[56] K.A. Christensen, H. Livbjerg, A plug flow model for chemical reactions and aerosol nucleation and growth in an alkali-containing flue gas, Aerosol Sci Technol 33 (2000) 470–489, doi:10.1080/02786820050195331.

[57] N.K. Meyer, Particulate, black carbon and organic emissions from small-scale residential wood combustion appliances in Switzerland, Biomass Bioenergy 36 (2012) 31–42, doi:10.1016/j.biombioe.2011.09.023.

[58] O. Sippula, K. Hytönen, J. Tissari, T. Raunemaa, J. Jokiniemi, Effect of wood fuel on the emissions from a top-feed pellet stove, Energy Fuels 21 (2007) 1151–1160, doi:10.1021/ef060286e.

[59] O. Sippula, T. Lind, J. Jokiniemi, Effects of chlorine and sulphur on particle formation in wood combustion performed in a laboratory scale reactor, Fuel 87 (2008) 2425–2436, doi:10.1016/j.fuel.2008.02.004.

[60] T. Blomberg, A thermodynamic study of the gaseous potassium chemistry in the convection sections of biomass fired boilers, Mater Corros 62 (2011) 635–641, doi:10.1002/maco.201005880.

[61] T. Blomberg, Correlation of the corrosion rates of steels in a straw fired boiler with the thermodynamically predicted trend of KOH(g) in the flue gases, Biomass Bioenergy 39 (2012) 489–493, doi:10.1016/j.biombioe.2012.01.016.

[62] H. Liu, H. Tan, Y. Liu, Z. Liu, L. Ma, M. Pourkashanian, et al., Study of the layered structure of deposit in a biomass-fired boiler (Case Study), Energy Fuels 25 (2011) 2593–2600, doi:10.1021/ef2003365.

[63] T. Blomberg, P. Makkonen, M. Hiltunen, Role of alkali hydroxides in the fireside corrosion of heat transfer surfaces, a practical approach, Mater Sci Forum 461–464 (2004) 883–890, doi:10.4028/www.scientific.net/MSF.461-464.883.